Vortex Lattice Method for Fan Tip-Flow Modeling

Valentin Caries, Christophe Montsarrat, Jérôme Boudet, Eric Lippinois

VORTEX LATTICE METHOD FOR FAN TIP-FLOW MODELING

V. Caries[1,3] *- C. Montsarrat*[2] *- J. Boudet*[1] *- E. Lippinois*[3]

[1]Univ Lyon, Ecole Centrale de Lyon, CNRS, Univ Claude Bernard Lyon 1, INSA Lyon, LMFA, UMR5509, 69130, Ecully, France; valentin.caries@ec-lyon.fr; jerome.boudet@ec-lyon.fr
[2]KTH Royal Institute of Technology, Stockholm, Sweden; cmon@kth.se
[3]Safran Aircraft Engine, Moissy-Cramayel, France; eric.lippinois@safrangroup.com

ABSTRACT

In the present work, a low-fidelity three-dimensional approach has been developed for the prediction of the flow around shrouded rotors. This method is to be used in the initial steps of design, for a wide exploration of the design space, including disruptive geometries, at minimal cost. The present approach is based on the vortex lattice method. First, the formulation on rotating geometries is validated by comparison with experiments. The Prandtl-Glauert correction is introduced to account for mild compressibility effects. A discretized approach is proposed to model the casing and simulate the tip-leakage flow. The results are discussed for different tip-gap sizes. A periodic boundary condition is also proposed and validated. This condition, together with programming techniques, decreases the computational and memory costs of the method. On average, a computation takes approximately one second to execute in real time. Finally, the method is applied to a shrouded fan configuration and the influence of the tip-gap size is analyzed.

KEYWORDS

VORTEX LATTICE METHOD, TIP-LEAKAGE FLOW, FAN

1 INTRODUCTION

For any engine manufacturer, designing a new rotating element is always a challenge. The reduction of aerodynamic losses is crucial for improving propulsive efficiency and specific fuel consumption. It is essential to correctly predict all physical phenomena at each design iteration. The tools must be versatile to adapt to disruptive geometries while remaining accurate and robust. The aerodynamic design process for a new blade geometry is complex, often involving various degrees of modeling fidelity. One-dimensional, meridional, and three-dimensional (3D) approaches are typically used. However, the development of disruptive technologies that could reduce losses presents many challenges for these modeling methods. Low-fidelity methods are often based on correlations obtained from a limited set of experimental setups, potentially far from the new designs envisioned. Reynolds-averaged Navier-Stokes (RANS) simulations use turbulence models that are often established on elementary configurations far from industrial cases. This might lead to a misprediction of the vortex structures and unphysical behaviors. For these reasons, high-fidelity methods such as large-eddy simulation (LES) are becoming increasingly popular, with lattice Boltzmann methods (LBM) being a possible approach. However, their high computational cost prevents them from being used in the early design phases. To reduce the assumptions in low-fidelity methods, using models based on general equations instead of correlations can be beneficial. This approach enables iterating through new geometries and aerodynamic conditions during the design process, with robust predictions. Empirical correlations are then used only when necessary, targeting specific phenomena and applications. This solution makes it easier to evaluate the limitations of a model.

1.1 Vortex Lattice Method

Theorized in the 1930s and named by Falkner (1943), the vortex lattice method (VLM) is a generalization of the lifting line theory formulated by Prandtl (1918). Here, the surface is both chordwise and spanwise discretized by vorticity panels. Thus, it is possible to solve potential 3D flows around bodies with low aspect ratios. VLM can be considered as a family of panel methods in which the thickness problem is not addressed. Usually, the slip boundary condition is applied to the camber surface, assuming a thin body. The computed loading corresponds to the pressure-difference between the pressure and the suction sides of the real body.

Historically, this method has been extensively used between the 1960s and the 1980s in the design of external aerodynamic elements, with codes like NASA's VORLAX software created by Miranda et al. (1977). The surface formulation of the VLM represented important advantages in memory cost for storing meshes, but also in CPU cost for solving the linear system. Past studies have proven its interest in propeller applications. For example, Masquelier (1982) and Kobayakawa and Onuma (1985) used it on propellers with helical horseshoe vortices (HSV). Counter-rotating propellers were modeled by Lesieutre and Sullivan (1985). VLM calculations were even performed for marine ducted propellers. In these studies, the casing was modeled with added source singularities by Houten (1986), while McHugh (1997) directly solved the casing with vortex elements. More recently, Colmenares et al. (2015) used unsteady VLM for vertical take-off and landing (VTOL) aircraft applications. Fei et al. (2021) applied it to propellers at incidence. On the other hand, to the best of our knowledge, no studies have been conducted on ducted turbomachinery applications.

The assumptions of incompressibility and irrotationality inherent in this method are restrictive. Models to reduce these constraints exist. Şugar Gabor et al. (2016) proposed a non-linear VLM approach to take into account viscous effects at high incidence. The Prandtl-Glauert (1928) correction has historically been used to extend the range of application of the VLM to Mach numbers up to ~ 0.6.

Finally, this method is of particular interest for simulating secondary flows in turbomachinery applications. As Denton (1993) has shown, these flows can cause up to one-third of the losses in a compressor. Among them, the tip-leakage flow (TLF) has probably the greatest aerodynamic impact and harm. This flow arises from the transfer of circulation from the blade to the main flow. The generation of the tip-leakage vortex (TLV) can also be seen as the roll-up of the leakage flow induced through the tip clearance by the pressure-difference on the blade. Lakshminarayana and Horlock (1963) were among the first to model the TLV using the lifting-line theory. It led to good predictions of the TLV circulation compared to the experiments. However, for gap sizes smaller than the chord length, this model overestimated the drag coefficient. The authors suggested that viscous effects were no longer negligible. More recently, Montsarrat (2021) applied the VLM to an isolated blade with a tip-gap. Good predictions with respect to experiments were obtained by introducing a viscous diffusion model based on two Lamb-Oseen's analytical vortices.

This paper aims at evaluating the VLM ability to perform influence studies during the early design phases, for configurations with axi-symmetric geometries and a casing. Specifically, the goal is to validate the implementation of the *PyLiSuite* VLM software and evaluate its CPU cost.

2 NUMERICAL METHOD

2.1 General Equations

The VLM model used in *PyLiSuite* comes from the theory presented by Katz and Plotkin (2004). It is used to compute the aerodynamic load on bodies in an inviscid, irrotational, and incompressible flow. Thus, the velocity vector is defined by the velocity potential $\mathbf{Q} = \nabla\Phi$. The Laplace equation is solved in the inertial reference frame:

$$\nabla^2\Phi = 0 \tag{1}$$

Among the different types of singularities available to solve the Laplace equation (1), the VLM uses vortices of constant intensity Γ mapped on the body surface. In *PyLiSuite*, two types of vortex singularities are implemented, as shown in Fig. 1. First, vortex rings are distributed on the whole structured grid, except at the trailing edge (TE). They are composed of four vortex segments. At the TE, HSV model the wake with pairs of semi-infinite vortex lines, called legs. At the walls, the Neumann boundary condition of non-penetration is applied to solve the problem. At each collocation point on the surface, the normal component of the flow velocity must be zero. The flow velocity is the sum of the velocities induced by the vortex elements and the unperturbed velocity (called kinematic velocity):

$$\nabla\left(\sum_{j=1}^{n\times m}\Phi_{\Gamma_j}+\Phi_k\right)\cdot\mathbf{n} = \left(\sum_{j=1}^{n\times m}\mathbf{Q}_{\Gamma_j}+\mathbf{Q}_k\right)\cdot\mathbf{n} = 0 \tag{2}$$

n and m are respectively the chordwise and spanwise cell numbers. The velocity induced by each vortex segment on a collocation point C is computed by the Biot-Savart law:

$$\mathbf{Q}_\Gamma = \frac{\Gamma}{4\pi}\frac{\mathbf{r_1}\times\mathbf{r_2}}{|\mathbf{r_1}\times\mathbf{r_2}|^2}\mathbf{r_0}\cdot\left(\frac{\mathbf{r_1}}{r_1}-\frac{\mathbf{r_2}}{r_2}\right) \tag{3}$$

Fig. 1(a) shows the notations used in equation (3). The boundary condition (2) for each collocation point i leads to a linear system to solve, where the circulation distribution is the unknown:

$$\sum_{j=1}^{n\times m} a_{ij}\Gamma_j = -\mathbf{Q}_{ki}\cdot\mathbf{n}_i \tag{4}$$

Where a_{ij} is the influence coefficient computed by equation (3) for the j-th vortex element on the i-th collocation point. At this point, the solution is not unique. The Kutta condition must be applied. In VLM, this condition is implicit. No additional equation is required, but the positions of (i) the collocation points and (ii) the heads of the HSV are critical to impose a zero circulation at the TE. Although Lan (1974) proposed a positioning model for complex geometries, the simple Pistolesi (1937) model, more commonly called the "$1/4 - 3/4$ *rule*", is used in *PyLiSuite*. As proven by James (1972), this model is remarkable for its simplicity and accuracy. It consists of placing the heads of the vortex elements and the collocation points at respectively $1/4$ and $3/4$ of the cell length. This choice is physically meaningful since, for a thin airfoil, the aerodynamic center is located at $1/4$ chord from the leading edge (LE). This echoes the placement of the vortex head, whose role is to generate lift on each panel. Fig. 1(b) illustrates the discretization of a thin lifting surface with vortex elements. The use of HSV at the TE only avoid stability issues due to interactions between the HSV legs and downstream singularities.

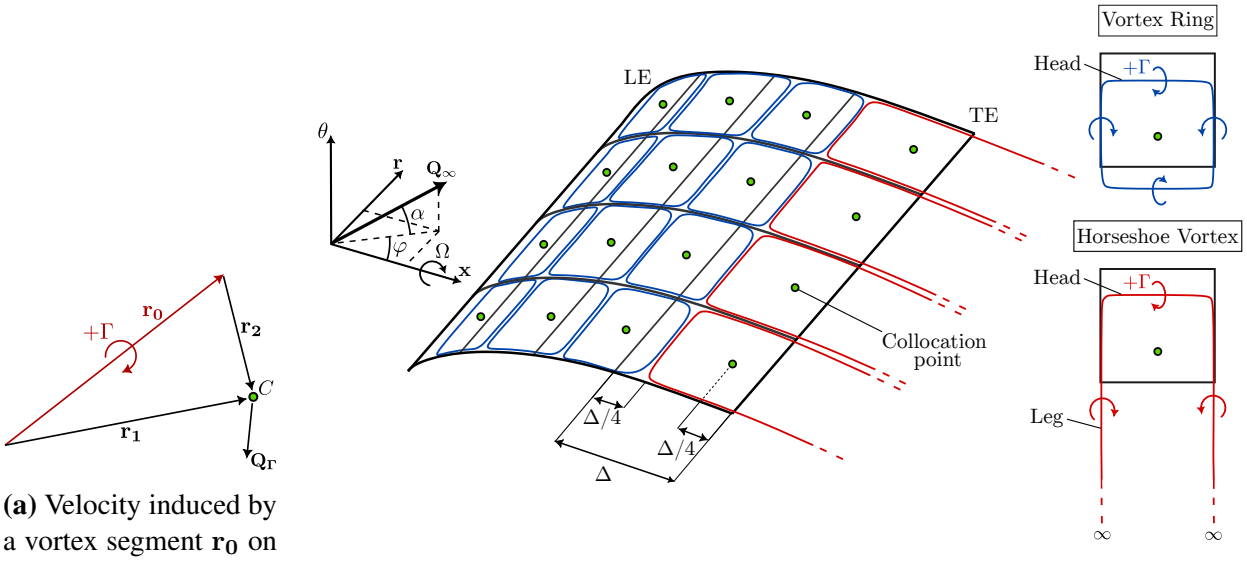

(a) Velocity induced by a vortex segment $\mathbf{r_0}$ on a collocation point C.

(b) Discretized camber surface.

Figure 1: VLM surface discretization.

2.2 Kinematic Velocity

The kinematic velocity in the body frame of reference, at a given collocation point, is decomposed into the sum of the freestream velocity $\mathbf{Q}_\infty$ and the velocity induced by the rotation of the blade:

$$\mathbf{Q}_k = \mathbf{Q}_\infty + \mathbf{\Omega} \times \mathbf{r} \tag{5}$$

The velocities being expressed in the body reference frame, $\mathbf{Q}_\infty$ and $\mathbf{\Omega}$ correspond respectively to the opposite of the translation and angular velocities of the body. Taking into account the azimuthal and radial flow angles, α and φ respectively, in cylindrical reference frame (see Fig. 1(b)), the freestream velocity of magnitude Q_∞ is expressed as:

$$\mathbf{Q}_\infty = Q_\infty \begin{pmatrix} \cos\alpha\cos\varphi \\ \cos\alpha\sin\varphi \\ \sin\alpha \end{pmatrix} \tag{6}$$

In cylindrical coordinates, the freestream velocity is independent of the azimuthal position of the blade. Expressing equations (5) and (6) in Cartesian coordinates, the kinematic velocity becomes:

$$\mathbf{Q}_k = \begin{pmatrix} Q_\infty\cos\alpha\cos\varphi \\ Q_\infty\cos\alpha\sin\varphi\cos\theta - (Q_\infty\sin\alpha + \Omega r)\sin\theta \\ Q_\infty\cos\alpha\sin\varphi\sin\theta + (Q_\infty\sin\alpha + \Omega r)\cos\theta \end{pmatrix} \tag{7}$$

2.3 Periodicity Condition

For applications with numerous blades around the circumference, the size of the linear system could become significant. It could drastically increase the CPU and memory cost of the calculation, decreasing the interest of this low-fidelity approach. A generalization to axi-symmetric geometries of the periodicity condition proposed by Montsarrat (2021) in his thesis is implemented. Assuming the flow is identical around each blade, the principle of this condition is to solve the linear system of equation (4) only for a single blade. The other periodic blades are only taken into account when

calculating the influence coefficients. In the general form, without the periodicity condition, the velocity induced by the vortex elements is:

$$\mathbf{Q}_\Gamma \cdot \mathbf{n} = \sum_{k=1}^{N} \sum_{i=1}^{n^{(k)}} \sum_{j=1}^{m^{(k)}} a_{ij}^{(k)} \Gamma_{ij}^{(k)} \tag{8}$$

Where N is the blade number, n and m the chordwise and spanwise cell numbers of a given k blade. This leads to an influence coefficient matrix of size $\left(\sum_{k=1}^{N} n^{(k)} m^{(k)}\right)^2$. Assuming the loading is identical on the N different blades, the periodic boundary condition writes:

$$\mathbf{Q}_\Gamma \cdot \mathbf{n} = \sum_{k=1}^{N} \sum_{i=1}^{n^{(1)}} \sum_{j=1}^{m^{(1)}} a_{ij}^{(k)} \Gamma_{ij}^{(1)} \tag{9}$$

This has the effect of drastically decreasing the computation cost for simulations using numerous blades. The influence coefficient matrix keeps a size equivalent to the single-bladed case, $\left(n^{(1)} m^{(1)}\right)^2$. Thus, the CPU cost to solve the linear system is considerably reduced. The cost of computing the influence coefficients is also scaled down. Finally, since it is only necessary to store the mesh and circulations for a single blade, the memory cost of the simulation is also reduced.

2.4 Compressibility Effects

As described earlier, using the standard VLM for flow fields of Mach numbers above ~ 0.3 is incorrect due to compressible effects that are no longer negligible. The Prandtl-Glauert correction is implemented to allow the use of the VLM at higher subsonic Mach numbers. In the linearized equation of small-disturbance for compressible flows (see Katz and Plotkin (2004)), by taking into account the total velocity defined in equation (5), one can derive Prandtl-Glauert correction for the three coordinates:

$$x_{PG} = \frac{x}{\sqrt{1 - \mathrm{Ma}_x^2}}, \quad y_{PG} = \frac{y}{\sqrt{1 - \mathrm{Ma}_y^2}}, \quad z_{PG} = \frac{z}{\sqrt{1 - \mathrm{Ma}_z^2}} \tag{10}$$

Where Ma_x, Ma_y and Ma_z are the Mach numbers based on each component of the total velocity. This correction is applied on the nodes of the blade mesh. The initial geometry is stretched in the three directions of space according to the Mach number vector components. For instance, for a rotor, the difference in intensity of the compressibility effects between the root and the tip of the blade is taken into account. This correction extends the VLM scope up to $\mathrm{Ma} \sim 0.6$.

2.5 Post Treatment

Once the linear system is solved and the circulation distribution on the blade computed, the load distribution ΔC_p can be calculated. The pressure-difference distribution is given by:

$$\Delta C_p \approx -2 \left(\frac{\mathbf{Q}_\Gamma + \mathbf{Q}_k}{\mathbf{Q}_k} \right)^2 \tag{11}$$

Finally, the lift coefficient is derived from the Kutta-Jukowski theorem:

$$C_L = \frac{\Gamma_{tot}}{\frac{1}{2} Q_k c\, b} \tag{12}$$

Where Γ_{tot}, c and b are respectively the total circulation computed by the linear system, the chord and the span lengths.

3 VALIDATIONS

3.1 Hover Rotor

First, the *PyLiSuite* code is evaluated on an axi-symmetric configuration. The reference configuration is the experimental setup of Caradonna and Tung (1981). This configuration models the hovering flight of a helicopter. It involves two untwisted and untapered NACA0012 blades with aspect ratio $\mathcal{AR} = 6$. They rotate at angular velocity Ω, with a fixed angle of attack α. Fig. 2 shows the numerical setup used. The data available allow plotting the C_p profiles at different spanwise positions. Since the VLM only provides the wall pressure-difference, the experimental ΔC_p is computed by interpolating the suction and pressure side data and differentiating the values at the same axial positions.

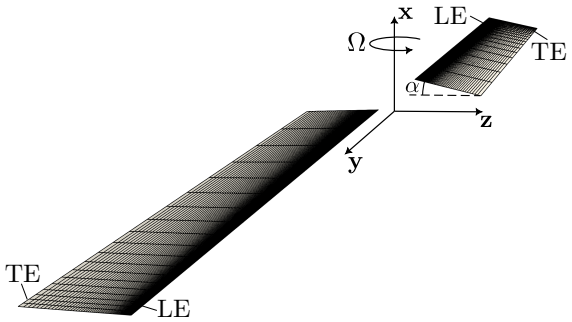

Figure 2: Structured mesh used on Caradonna and Tung (1981) configuration.

A grid convergence study allowed setting the appropriate resolution of the structured mesh. Two flat plates composed of 58×19 quadrilateral panels are used to model the uncambered NACA0012 blades. Chordwise and spanwise clusterings are used to better capture the high-gradient regions.

A first validation step is to compare the results for an angular velocity of 650 rpm, which corresponds to a tip Mach number of 0.23. Thus, the assumption of incompressibility is satisfied. Fig. 3(a) compares the pressure-difference distributions for three different spanwise positions and for two different angles of attack, between the experiment and the simulation. *PyLiSuite* provides a good prediction of the levels, and the increase in load with incidence is correctly captured. The numerical predictions show a decrease in loading when approaching the tip of the blade. This is an expected result since the circulation at the blade tip is transferred to the TLV. However, this behavior is not always represented in the experimental data. The lack of knowledge about the uncertainty of the measurements prevents a more detailed analysis of this difference.

Fig. 3(b) compares the *PyLiSuite* results with the experiment for an angular velocity of 1750 rpm. This corresponds to a Mach number of 0.61 at the blade tip. Thus, the Prandtl-Glauert correction is used. *PyLiSuite* achieves a fairly good prediction of ΔC_p for different angles of incidence. However, the overestimation of the results compared to the experimental data is more significant. This could be due to the construction of the HSV that does not allow for wake roll-up. According to the Kutta-Joukowski theorem, the wake generates excess lift when it is not locally aligned with the flow. As recommended by Katz and Maskew (1988), one way to tackle this effect is to employ an unsteady free wake approach. Implementing a helical HSV technique in the style of Masquelier (1982) and Kobayakawa and Onuma (1985) is another option that could lead to improved results.

3.2 Periodicity Condition

The verification of the implementation of the periodicity conditions is carried out. Two calculations on the Caradonna and Tung (1981) configuration are performed. The first one corresponds

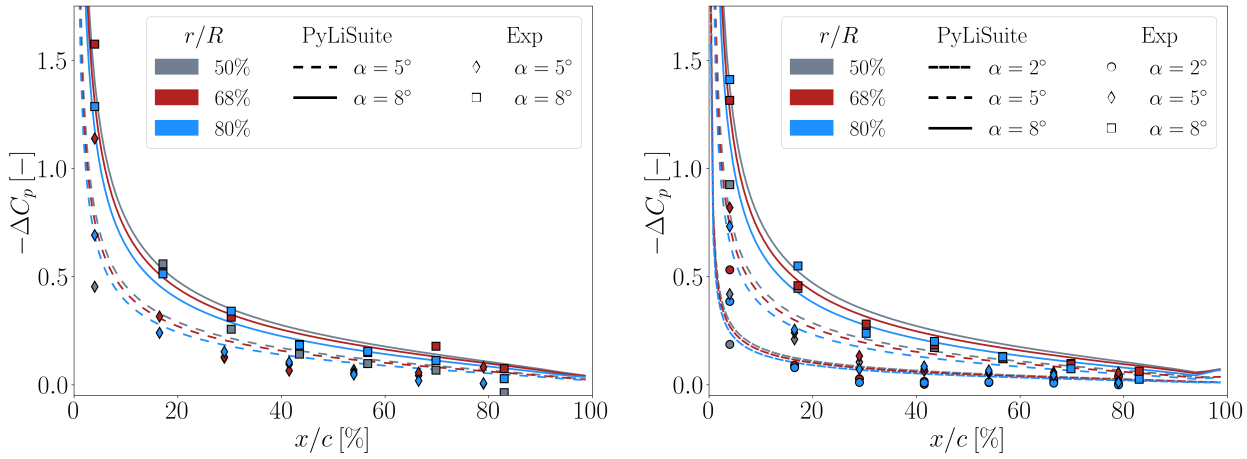

(a) $\Omega = 650$ rpm **(b)** $\Omega = 1750$ rpm

Figure 3: Pressure coefficient difference at various spanwise positions (colors), between experiment (markers) and *PyLiSuite* (lines), for different angles of attack.

to the results shown in Fig. 3(a) for an incidence angle of 8°. The second one refers to the same operating point and uses the periodicity condition. Thus, only one blade is simulated, the second being taken into account through the calculation of the influence coefficients. Fig. 4(a) shows the pressure coefficients difference ΔC_p for the two simulations. Both approaches give equivalent results. Thus, the implementation of the periodicity condition is validated. Fig. 4(b) shows the speed-up factor for solving a fictitious case based on the Caradonna and Tung (1981) configuration with a varying number of blades. This ratio is calculated as the CPU time necessary to compute a simulation with all the blades meshed compared to the one using the periodicity condition. It is clear that the use of the periodicity condition is interesting for simulations with numerous blades. An order of magnitude in acceleration is gained for a case of only 5 blades. The time savings are then considerable for a higher number of blades. Compared to CFD methods such as RANS approaches where a speed-up proportional to the number of blades is usually achievable at best, the speed-up observed here is notably higher. For instance, with 20 blades, the speed-up factor is greater than 100.

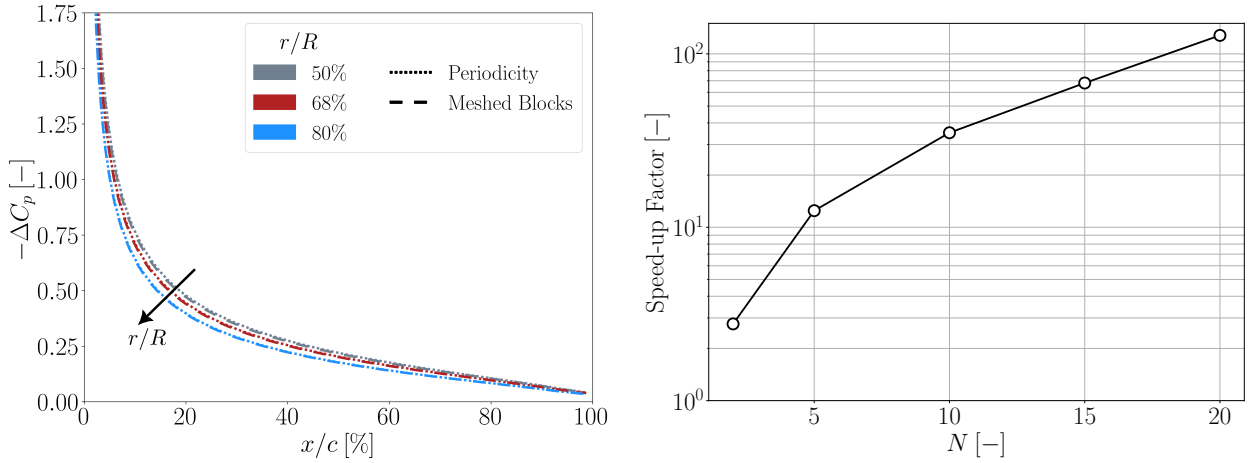

(a) Pressure coefficient difference at various spanwise positions, for periodic and fully meshed cases.

(b) Speed-up factor when using periodicity condition. Evolution with the number of blades.

Figure 4: Verification and performance of the periodicity condition.

3.3 Casing Effect

In order to apply VLM to turbomachines, the implementation of a casing model is an essential step. For linear cascades, Fig. 5(a) shows two possible approaches. One way is to use the mirror symmetry condition as Lakshminarayana and Horlock (1967) did for their split wing. Two blades are placed at a distance of twice the size of the tip-gap τ. This approach, which was already developed in Montsarrat (2021) thesis, was validated and proved its relevance for linear cascade applications. However, this method is restricted to infinitely long plane casings. An alternative solution is to use vortex elements to mesh the casing and apply the non-penetration boundary condition, as previously done by McHugh (1997). This approach allows for modeling any casing geometry. A linear cascade configuration is investigated to verify the implementation of the meshed casing. The simulated blade geometry corresponds to an uncambered airfoil with an aspect ratio $\mathcal{AR} = 2.6$. The flow is uniform with a velocity magnitude $Q_\infty = 40\,\mathrm{m/s}$ and an angle of attack $\alpha = 10°$. The blade mesh has been densified near the tip, following the rule recommended by Montsarrat (2021) in his thesis:

$$\frac{\tau}{\Delta_{0,b}} > 2 \tag{13}$$

Here, $\Delta_{0,b}$ is the spanwise size of the first cell at the blade tip. After conducting a mesh convergence study, the blade mesh size is 49×63 cells. As shown in Fig. 5(a), a square surface of size $150c$ is used to discretize the casing. This large size is intentionally chosen to approach the behavior of an infinitely long casing as for the mirror symmetry condition. The mesh is refined near the blade using a cosine distribution that satisfies the condition in equation (13).

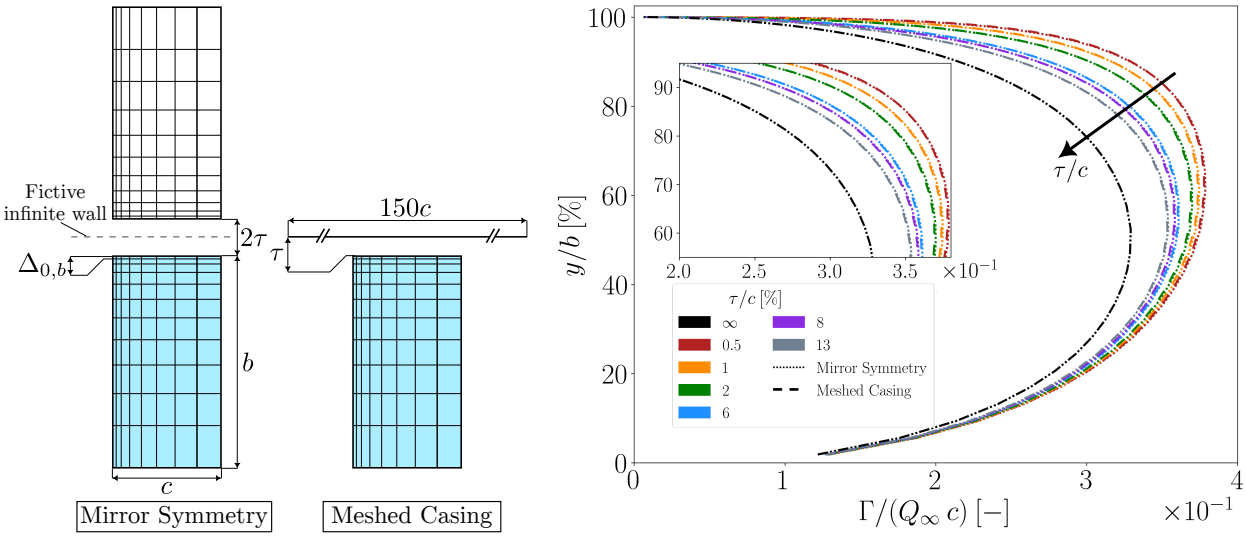

(a) Scheme of the two simulated configurations. The blade of interest is colored in blue.

(b) Spanwise circulation distribution for various tip-gap sizes. Mirror symmetry (dotted) vs meshed casing (dashed).

Figure 5: Comparison of the mirror symmetry and the meshed casing approaches.

Fig. 5(b) compares the spanwise circulation distributions between the two approaches, for different tip-gap sizes. The influence of the casing is negligible below 15% span for both approaches and the circulations match the case with no casing ($\tau/c \to \infty$). Above, the casing amplifies the circulation, especially as the tip-gap size decreases. Finally, it should be noted that both approaches provide very similar results, thereby validating the use of the meshed casing approach in VLM.

To replicate the S2L experimental scenario, a hub with zero clearance is added. This setup was studied by Deveaux (2020) to examine TLF. The TLV circulation was measured at 5% chord length downstream of the blade. In the simulation, it is assumed that all generated circulation is transferred to the TLV. Table 1 shows the TLV circulation values in comparison to the experimental results. As shown by Montsarrat (2021), viscous effects are not negligible for gap sizes smaller than 6%. Consequently, the present approach only considers $\tau/c \geq 6\%$. Reasonable agreements are observed for large gap values. Investigations at low gap values would require the introduction of a viscous model, such as the one proposed by Montsarrat (2021).

$\Gamma_{TLV}/(Q_\infty c)$ [−]	τ/c [%]	6	8	13
	Exp	0.440	0.480	0.460
	PyLiSuite	0.483	0.481	0.475

Table 1: TLV circulation compared to Deveaux (2020)'s S2L experiment.

4 RESULTS

4.1 Influence of the Tip-Gap Size on a Shrouded Fan Configuration

A parametric study on the tip-gap size is now carried out on a shrouded fan. Three uncambered blades, each with an aspect ratio $\mathcal{R} = 6$ and equally spaced are used. The blades are exposed to an incident axial flow of $200\,\mathrm{m/s}$ and held at a fixed stagger angle of $5°$. The angular velocity is set to 500 rpm. Hence, the corresponding blade tip Mach number is 0.60 and the computations use the Prandtl-Glauert correction. The blade's angle of incidence satisfies the assumption of small disturbances, ranging from $-2°$ at the root to $10°$ at the tip. The cylindrical hub and casing extend axially over 8 chord lengths, centered around the blades. After conducting a mesh convergence study, the blade mesh size is set to 49×63 cells with a spanwise cosine distribution, while the hub and casing meshes use 99×49 cells with a chordwise cosine distribution, to satisfy the condition of equation (13). The simulation models the entire geometry with a 120 degree sector. The remaining two sectors are taken into account with the periodicity condition.

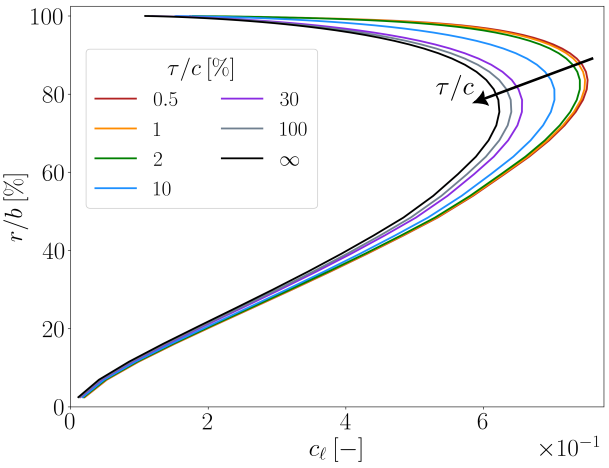

Figure 6: Lift coefficient along span for various tip-gap sizes.

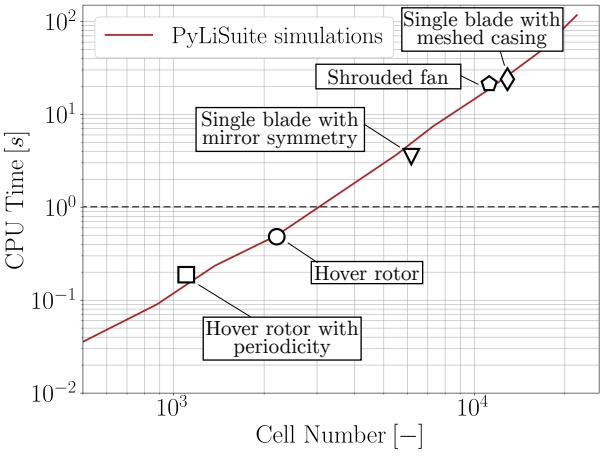

Figure 7: CPU time for a simulation as a function of the mesh size.

Fig. 6 shows the lift coefficient distribution in the spanwise direction. Decreasing the size of the tip-gap enhances lift generation in the upper half of the blade. However, as mentioned by Greitzer et al. (2004), for non-zero tip-gap sizes, the blade circulation is entirely transferred to the flow.

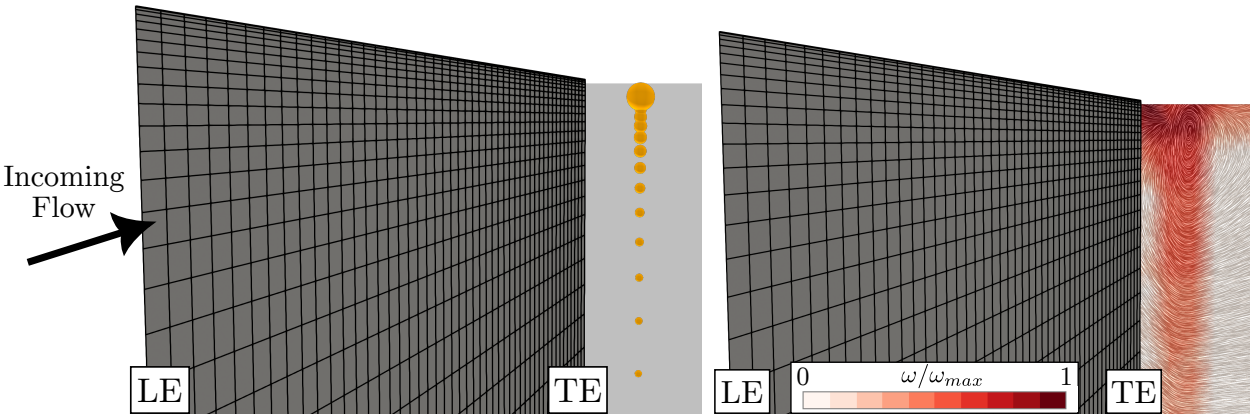

(a) Intersections of the HSV legs with the cutting plane, scaled by circulation.

(b) Normalized vorticity ω and streamlines in the cutting plane.

Figure 8: Cutting plane perpendicular to the main flow at 0.25c downstream of the blade. Simulation with $\tau/c = 1.0\%$.

Thus, the lift tends towards 0 at the tip of the blade. The same behavior is observed in the analysis conducted by McHugh (1997). Because the incidence approaches zero near the blade's root, the circulation and thus lift generation in that region vanishes. Fig. 8(a) shows the intersection points of the HSV legs with a cutting plane located at $0.25c$ from the TE. The HSV circulation is used to scale these points. The intensity increases for HSV legs located near the blade tip. As illustrated by Fig. 8(b), this high-intensity region corresponds to a swirling motion of the streamlines. This is related to the TLV, for which the highest levels of vorticity are found.

4.2 Optimization of the Computational Effort

PyLiSuite is a fully object-oriented Python code that has received special attention for computational cost and performance acceleration. The most resource-intensive operations, such as the calculation of the influence coefficients, are performed by wrapped Fortran routines. This allows for a speed-up compared to a full Python version, while benefiting from the ease of implementation offered by the object-oriented Python language. The remaining operations are performed using packages that are also optimized for vector computing. A comparative study showed that the lower-upper decomposition algorithm is the most efficient for solving the linear system. Fig. 7 summarizes the CPU time required to perform a simulation using *PyLiSuite* as a function of the number of cells. The different cases presented in this article are indicated. To achieve mesh convergence, most applications so far have required blade meshes with several thousand cells. This leads to a computation time of the order of the second. This is satisfactory for a low-fidelity of approach, to be used in preliminary design phase. When using a meshed casing, the number of elements increases strongly, making the CPU time rise to the order of 10 to 20 seconds. It might be relevant in the future, when using larger meshes, to consider parallelization.

5 CONCLUSION

A VLM strategy has been developed to investigate tip-leakage flows in shrouded rotors. Specific methods have been introduced and validated to represent periodicity, mild compressibility effects, and the casing. Moreover, attention has been paid to CPU efficiency, with simulation times of the order of one second. Finally, a parametric study on the influence of tip-gap size in a shrouded fan has been presented.

Several ways of improvement are currently under investigation to reduce the impact of the underlying assumptions of the VLM strategy. To avoid the non-physical lift generation introduced by the wake misalignment with the freestream flow, an unsteady free wake model such as the one presented by Katz and Plotkin (2004) could be implemented. To better characterize the TLF at low tip-gap to chord ratio, Montsarrat (2021) viscous model would be relevant. Finally, future comparisons with experiments and high-fidelity simulations will provide a better insight into the accuracy of this method for turbomachinery applications.

NOMENCLATURE

Acronyms

CPU	Central Processing Unit
HSV	HorseShoe Vortex
LE	Leading Edge
LES	Large-Eddy Simulation
LBM	Lattice Boltzmann Method
RANS	Reynolds-Averaged Navier Stokes
TE	Trailing Edge
TLF	Tip-Leakage Flow
TLV	Tip-Leakage Vortex
VLM	Vortex Lattice Method

Greek symbols

α	Azimuthal angle
Γ	Circulation intensity
Δ	Cell dimension
ΔC_p	Pressure coefficient difference
θ	Azimuthal coordinate angle
τ	Tip gap size
Φ	Velocity potential
φ	Radial angle
$\mathbf{\Omega}$	Angular velocity

Latin symbols

a_{ij}	Influence coefficients matrix
b	Span
c	Chord
C_L	Lift coefficient
m	Spanwise cell number
Ma	Mach number
n	Chordwise cell number
$\mathbf{n}$	Normal vector
$\mathbf{Q}$	Velocity vector
Q	Velocity magnitude
$\mathbf{r}$	Radial coordinate vector
x	Axial coordinate
y	Spanwise coordinate
z	Pitch-wise coordinate

Subscripts

Γ	Induced by a vortex element
∞	Freestream
PG	Prandtl-Glauert
k	Kinematic
x	Axial component
y	Spanwise component
z	Pitch-wise component

References

Caradonna, F. X. and Tung, C. (1981). Experimental and Analytical Studies of a Model Helicopter Rotor in Hover. *NASA Technical Memorandum*, page 60.

Colmenares, J. D., López, O. D., and Preidikman, S. (2015). Computational Study of a Transverse Rotor Aircraft in Hover Using the Unsteady Vortex Lattice Method. *Mathematical Problems in Engineering*, 2015:1–9.

Denton, J. D. (1993). Loss Mechanisms in Turbomachines. In *Volume 2: IGTI Scholar Award*, Cincinnati, Ohio, USA. American Society of Mechanical Engineers.

Deveaux, B. (2020). *Analyse et contrôle de l'écoulement de jeu d'une aube fixe isolée*. PhD thesis, Ecole Nationale Supérieure d'Arts et Métiers.

Falkner, V. M. (1943). The Calculation of Aerodynamic Loading on Surfaces of Any Shape. *His Majesty's Stationery Office*.

Fei, X., Litherland, B. L., and German, B. J. (2021). Development of an Unsteady Vortex Lattice Method to Model Propellers at Incidence. *AIAA Journal*, pages 1–13.

Glauert, H. (1928). The effect of compressibility on the lift of an aerofoil. *Proceedings of The Royal Society A: Mathematical, Physical and Engineering Sciences*, 118:113–119.

Greitzer, E. M., Tan, C. S., and Graf, M. B. (2004). *Internal Flow: Concepts and Applications*. Cambridge University Press, first edition.

Houten, R. V. (1986). Analysis of ducted propellers in steady flow. *Airflow Research And Manufacturing Corp*, page 65.

James, R. M. (1972). On the remarkable accuracy of the vortex lattice method. *Computer Methods in Applied Mechanics and Engineering*, 1(1):59–79.

Katz, J. and Maskew, B. (1988). Unsteady low-speed aerodynamic model for complete aircraft configurations. *Journal of Aircraft*, 25(4):302–310.

Katz, J. and Plotkin, A. (2004). Low-Speed Aerodynamics, Second Edition. *Journal of Fluids Engineering*, 126(2):293–294.

Kobayakawa, M. and Onuma, H. (1985). Propeller aerodynamic performance by vortex-lattice method. *Journal of Aircraft*, 22(8):649–654.

Lakshminarayana, B. and Horlock, J. H. (1963). Tip-Clearance Flow and Losses for an Isolated Compressor Blade. *Physics, Engineering*.

Lakshminarayana, B. and Horlock, J. H. (1967). Leakage and Secondary Flows in Compressor Cascades. *HM Stationery Office*, page 60.

Lan, C. E. (1974). A Quasi-Vortex-Lattice Method in Thin Wing Theory. *Journal of Aircraft*, 11(9):518–527.

Lesieutre, D. J. and Sullivan, J. P. (1985). The Analysis of Counter-Rotating Propeller Systems. In *General Aviation Aircraft Meeting and Exposition*, pages 564–575.

Masquelier, M. L. (1982). *Application of the Vortex-Lattice Method to Propeller Performance Analysis*. PhD thesis, Air Force Institute of Technology.

McHugh, G. P. (1997). *Advances in Ducted Propulsor Analysis Using Vortex-Lattice Lifting-Surface Techniques*. PhD thesis, Massachusetts Institute of Technology.

Miranda, L. R., Elliot, R. D., and Baker, W. M. (1977). A Generalized Vortex Lattice Method for subsonic and supersonic flow applications. *NASA Contractor report*.

Montsarrat, C. (2021). *Tip-leakage flow modelling in axial compressors*. PhD thesis, Ecole Centrale de Lyon, Ecully.

Pistolesi, E. (1937). Considerations Respecting the Mutual Influence of Systems of Airfoils. *Gesammelte Vorträge der Hauptversammlung der Lilienthal-Gesellschaft*.

Prandtl, L. (1918). Tragflügeltheorie. I. Mitteilung. *Nachrichten von der Gesellschaft der Wissenschaften zu Göttingen, Mathematisch-Physikalische Klasse*, pages 451–477.

Şugar Gabor, O., Koreanschi, A., and Botez, R. M. (2016). A new non-linear vortex lattice method: Applications to wing aerodynamic optimizations. *Chinese Journal of Aeronautics*, 29(5):1178–1195.